Materials Advances

ROYAL SOCIETY OF CHEMISTRY

PAPER

View Article Online
View Journal

Cite this: DOI: 10.1039/d6ma00109b

Breathable, water-repellent γ-MnOOH nest production by vapor-assisted conversion

Takahiro Kozawa, *[a] Kayo Fukuyama,[a] Minoru Osada [b] and Hiroya Abe[a]

Bird nests, formed by slender, semi-flexible twigs, are lightweight, freestanding porous frameworks with excellent permeability to gases and liquids. Translating this concept to microscale inorganic materials promises a broad impact on engineering and biomedical applications. However, constructing freestanding porous architectures from rigid one-dimensional (1D) particles remains challenging due to the directional processing and sparse interparticle contacts. To overcome these limitations, an *in situ* route for growing high-aspect-ratio 1D crystals within powder compacts is developed, yielding abundant, randomly oriented interparticle contacts. Exposing $MnCO_3$ to H_2O_2/H_2O vapor at 200 °C drives vapor-assisted oxidative conversion to γ-MnOOH, producing hierarchical, nest-like porous frameworks. The resulting γ-MnOOH bodies exhibit high water permeability (≈140 L m^{-2} h^{-1}) and rapid evaporation (0.45–0.56 L m^{-2} h^{-1} at 40 °C), and simple postsynthetic surface modification imparts water repellency (contact angle of 169°). Because oxyhydroxides are versatile precursors for ceramic oxides, this approach provides a platform for entangled, binder-free inorganic architectures. This establishes a scalable and straightforward route to breathable porous materials, guided by the design logic of nature.

Received 23rd January 2026,
Accepted 14th April 2026

DOI: 10.1039/d6ma00109b

rsc.li/materials-advances

1. Introduction

Bird nests are a remarkable example of natural engineering, in which slender, semi-flexible twigs are intricately interwoven by frictional and geometrical interactions.[1–3] These structures form lightweight frameworks that remain permeable and resilient owing to their loosely entangled architecture.[4] This bio-inspired principle suggests a route to freestanding, porous bodies in which structural integrity emerges from numerous non-directional contacts rather than from binders or sintered necks.[5]

Translating this concept to microscale inorganic materials would enable breathable, robust architectures for thermal management, acoustic damping, mass transport, and environmental interfaces.[6–9] Furthermore, employing biocompatible materials could provide cells with favorable microenvironments as biomedical scaffolds.[10] However, constructing freestanding porous architectures from rigid one-dimensional (1D) particles remains a formidable challenge. While additive manufacturing and freeze casting can impose complex shapes or align anisotropic building blocks,[11–15] they inherently rely on directional deposition or templated freezing, which promotes mechanical anisotropy. Moreover, interparticle contacts are sparse and weak in the absence of mechanical interlocking.[16]

To overcome the limitations of directional processing and sparse interparticle contacts inherent to the prevailing methods, we propose an *in situ* route that generates abundant, randomly oriented contacts by growing high-aspect-ratio 1D crystals within powder compacts. This approach proceeds *via* the vapor-assisted oxidative conversion of manganese carbonate ($MnCO_3$) to manganese oxyhydroxide (γ-MnOOH) at 200 °C in H_2O_2/H_2O vapors (Fig. 1A). Growth within confined powder compacts produces randomly oriented, interwoven 1D crystals that self-organize into nest-like porous frameworks with hierarchical features (Fig. 1B). The resulting freestanding γ-MnOOH bodies exhibit high liquid permeability and rapid evaporation and can be rendered water-repellent *via* postsynthetic surface modification. Because oxyhydroxides serve as versatile precursors for subsequent transformations into ceramic oxides, this approach establishes a platform for entangled, binder-free inorganic architectures. Together, these results outline a simple, scalable route to breathable porous bodies guided by the design logic of nature.

2. Experimental

2.1. Synthesis of spherical $MnCO_3$ powder

Spherical $MnCO_3$ particles were synthesized *via* a controlled precipitation method.[17] Briefly, 0.52 mol of $(NH_4)_2CO_3$

[a] Joining and Welding Research Institute, The University of Osaka, 11-1 Mihogaoka, Ibaraki, Osaka 567-0047, Japan. E-mail: kozawa.takahiro.jwri@osaka-u.ac.jp; Tel: +81-6-6879-8656
[b] Institute of Materials and Systems for Sustainability (IMaSS) and Department of Chemistry, Nagoya University, Nagoya 464-8601, Japan

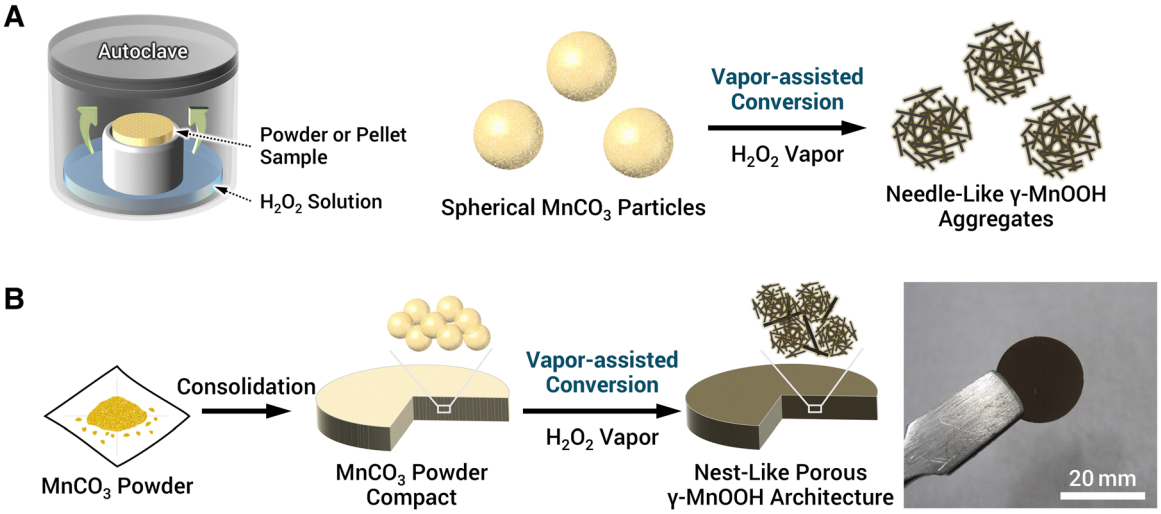

Fig. 1 Schematic illustration of a vapor-assisted conversion strategy for fabricating a porous γ-MnOOH framework. (A) Formation of needle-like γ-MnOOH aggregates from spherical $MnCO_3$ particles. (B) Development of nest-like porous γ-MnOOH architectures within the $MnCO_3$ powder compact.

(FUJIFILM Wako Pure Chemical) and 60 mL of 28% NH_4OH (FUJIFILM Wako Pure Chemical) were dissolved in water and diluted to a final volume of 500 mL. This carbonate solution was added dropwise to 500 mL of 0.5 M $MnSO_4$ (Kishida Chemical) under continuous stirring at a rate of 15 mL min^{-1}. After complete addition, the suspension was stirred for 1 h. The resulting $MnCO_3$ precipitate was collected by filtration, washed with water, and dried at 100 °C in an oven.

2.2. Vapor-assisted conversion of $MnCO_3$ powder

The as-prepared $MnCO_3$ powders were subjected to vapor-phase treatment using either water or H_2O_2 (FUJIFILM Wako Pure Chemical) as the vapor source. In a typical procedure, 5 mL of water or a 5–10% H_2O_2 solution was placed at the bottom of a PTFE-lined stainless-steel autoclave (internal volume: 50 cm^3). A PTFE support with a recessed top was used to hold 0.5 g of $MnCO_3$ powder above the liquid phase to avoid direct contact. The sealed autoclave was heated to 200 °C and maintained for 6 h. After cooling to room temperature, the treated powders were washed with water and ethanol and dried at 100 °C.

2.3. Fabrication of nest-like porous γ-MnOOH architecture

Nest-like porous γ-MnOOH architectures were fabricated *via* vapor-phase treatment of $MnCO_3$ powder compacts. The compacts were prepared *via* hydrothermal hot-pressing.[18] Wet $MnCO_3$ powder containing 15 mass% water was loaded into a cylindrical mold (inner diameter: 20 mm) and compressed at 100 MPa using PTFE-sealed pistons. The mold was externally heated to 120 °C and maintained for 2 h. After cooling, the compacts were demolded, dried, and polished to a thickness of 1.5 mm. Vapor-phase treatment was then performed at 200 °C for up to 16 h in a PTFE-lined autoclave (internal volume: 250 cm^3) using 20 mL of water or a 5–30% H_2O_2 solution. The compacts were placed on a support to avoid direct contact with the liquid. After treatment, the samples were dried at 100 °C. Hydrophobic modification was performed by vapor-phase silanization. The solid sample and trimethoxy(methyl)silane (KBM-13, Shin-Etsu Chemical) were placed in a steel-lined autoclave without direct contact and exposed to silane vapor at 100 °C for 2.5 h.

2.4. Characterization

Phase identification was performed using powder X-ray diffraction (XRD, D2 PHASER, Bruker AXS) with Cu Kα radiation at 30 kV and 10 mA. Data were collected with a step size of 0.02° (2θ) and a counting time of 0.5 s $step^{-1}$. Phase quantification was performed semi-quantitatively using the reference intensity ratio method with the DIFFRAC.EVA software (ver. 5.2.0.5, Bruker AXS). Morphological and microstructural analyses were conducted using scanning electron microscopy (SEM, JSM-6010LA, JEOL) and transmission electron microscopy (TEM, JEM-2100F, JEOL). Three-dimensional (3D) microstructural imaging was obtained using focused ion beam SEM (FIB-SEM, NB5000, Hitachi High-Tech), and 3D reconstructions were generated using Avizo software (ver. 2023.2). The pore size distributions were measured by mercury intrusion porosimetry (AutoPore V, Micromeritics), with the pore sizes calculated using the Washburn equation. The surface tension and contact angle of mercury were set to 485 mN m^{-1} and 130°, respectively. The surface functional groups were analyzed using Fourier-transform infrared spectroscopy (FTIR, IRSpirit, Shimadzu) in attenuated total reflectance mode. Contact angle measurements were performed by vertically dispensing a 10 μL droplet at 25 °C and capturing an image after 30 s, following the method described by Alkawareek *et al.*[19] The oil slurry used in the three-phase separation was prepared by mixing a lipophilic dye (Oil Red O, FUJIFILM Wako Pure Chemical) dissolved in linseed oil (FUJIFILM Wako Pure Chemical) with hydrophobically modified spherical Fe_3O_4 particles.

3. Results and discussion

3.1. Vapor-assisted conversion of $MnCO_3$ to interwoven γ-MnOOH nanorods

Hydrothermal vapor treatment of $MnCO_3$ in the presence of H_2O_2 induces γ-MnOOH formation *via* simultaneous decarboxylation, hydration, and oxidation. Manganese oxides catalyze liquid H_2O_2 decomposition, rapidly releasing oxygen at particle surfaces.[20,21] Consistently, $MnCO_3$ reacted immediately upon contact with liquid H_2O_2 (Fig. S1). To avoid premature reactions, $MnCO_3$ and H_2O_2 were spatially separated in a sealed autoclave (Fig. 1A). Spherical $MnCO_3$ particles (median diameter ≈2 μm) exposed to H_2O_2/H_2O vapor generated from 5% aqueous H_2O_2 at 200 °C developed surface protrusions within 0.5 h (Fig. 2A). After 1 h, they were converted into spherical aggregates composed of needle-like γ-MnOOH crystals and remained morphologically stable for 6 h. Powder XRD showed the progressive conversion of $MnCO_3$ to γ-MnOOH with Mn_3O_4 as a minor by-product (Fig. S2). Increasing the H_2O_2 concentration to 10% accelerated the conversion without altering the aggregate morphology (Fig. S3). In contrast, replacing H_2O_2 with water vapor markedly suppressed the formation of γ-MnOOH while facilitating the production of Mn_3O_4, yielding a mixture of spherical $MnCO_3$, needle-like γ-MnOOH, and polyhedral Mn_3O_4 (Fig. S4).

The reaction proceeds at the solid–gas interface, where γ-MnOOH nucleates and grows by consuming Mn^{2+} from $MnCO_3$. The progressive evolution from smooth $MnCO_3$ spheres to surface-nucleated γ-MnOOH nanorods (Fig. 2A) indicates an interface-mediated oxidative dissolution-reprecipitation mechanism, in which Mn^{2+} ions released at the $MnCO_3$ surface are oxidized and reprecipitate as γ-MnOOH; the preserved spherical aggregate morphology is consistent with a surface-confined reaction front advancing inward, rather than a bulk solid-state transformation. The crystals exhibited unidirectional elongation and freely interwove (Fig. 2B(a)). High-resolution TEM indicates preferential growth along ⟨101⟩ while exposing facets indexed as (1̄11) (Fig. S5), behavior commonly observed in liquid-phase syntheses.[22–24] Spontaneous branching occurs during vapor-induced growth (Fig. 2B(b)), consistent with reports on hydrothermal γ-MnOOH.[25–27] We infer that rapid tip-directed growth of sword-like nanorods along ⟨101⟩ is followed by tip-to-tip fusion to form branches.[27] Moiré fringes at the branch bases suggest slight lattice rotations or interplanar mismatches. Continuous H_2O_2 supply sustains rapid crystal growth, and the exposed (111)-type facets at rod tips (Fig. 2B(c)) are conducive to twin-plane formation at branching interfaces.[27] A poorly crystalline Mn-oxide layer (≈3 nm) was also observed on particle surfaces (Fig. S5), likely arising from electron-beam-induced oxidation during TEM imaging.[27] Under the synthesis conditions (200 °C, elevated pressure), such surface activity may influence Mn-oxide stability and phase evolution.

Under hydrothermal vapor conditions, γ-MnOOH formation proceeds *via* coupled redox and decarboxylation reactions. Vapor-phase H_2O_2 oxidizes Mn^{2+} in $MnCO_3$ while decomposing into hydroxyl radicals and ions:

$$MnCO_3 + H_2O_2 \rightarrow HO^{\bullet} + OH^- + [Mn^{3+}\cdots CO_3^{2-}] \quad (1)$$

The bracketed species denote the transient complex at the active site. The carbonate ion donates oxygen to the lattice and is released as CO_2, whereas hydroxide ions yield γ-MnOOH as follows:

$$OH^- + [Mn^{3+}\cdots CO_3^{2-}] \rightarrow \gamma\text{-MnOOH} + CO_2 \quad (2)$$

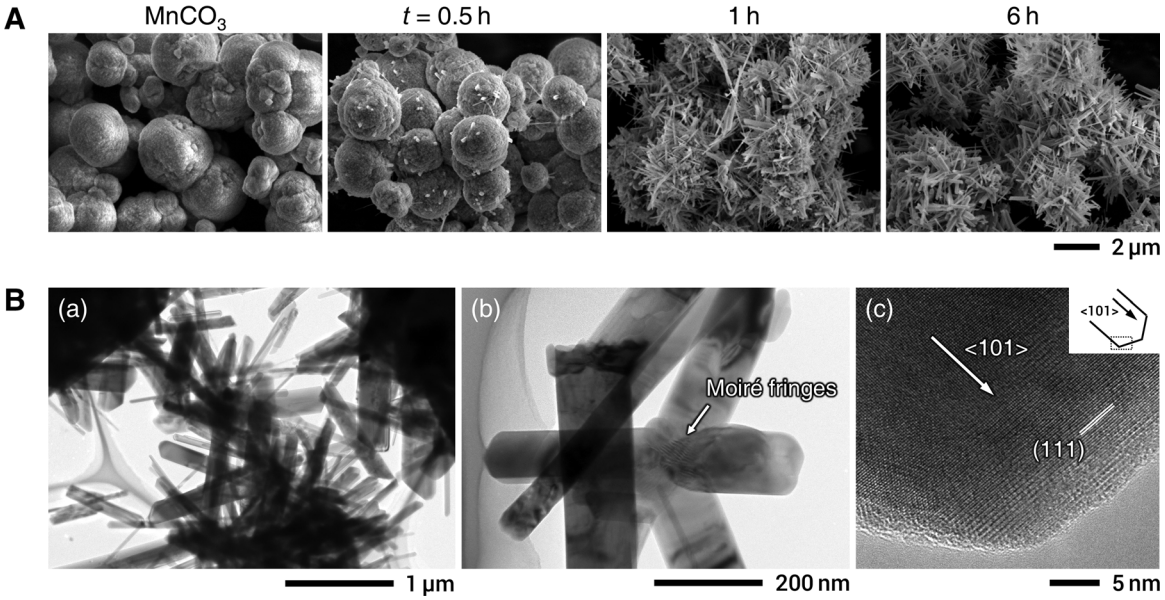

Fig. 2 Morphological evolution and nanoscale features of γ-MnOOH produced *via* vapor-assisted conversion. (A) SEM image sequence showing the transformation of spherical $MnCO_3$ in 5% H_2O_2 vapor. (B) TEM images of needle-like γ-MnOOH after 2 h in 10% H_2O_2 vapor: (a) overview, (b) branched nanorods, and (c) lattice-resolved tip.

Concurrently, hydroxyl radicals further oxidize adjacent $MnCO_3$:

$$HO^{\bullet} + MnCO_3 \rightarrow OH^- + [Mn^{3+}\cdots CO_3^{2-}] \quad (3)$$

Overall:

$$2MnCO_3 + H_2O_2 \rightarrow 2\gamma\text{-MnOOH} + 2CO_2 \quad (4)$$

The proposed involvement of $HO^{\bullet}$ is inferred from established literature on H_2O_2 decomposition over manganese oxides[20,21] and represents a working mechanistic hypothesis; direct verification remains a subject for future work. In the absence of H_2O_2, Mn^{2+} can be oxidized by molecular oxygen in water vapor.[28] Owing to its limited oxidizing power, this pathway favors Mn_3O_4 and the coexistence of Mn^{2+} and Mn^{3+} ions. In contrast, H_2O_2 vapor promotes further oxidation and hydration, ultimately producing γ-MnOOH.

This vapor-phase route directly generates nanoscale 1D materials from solid precursors, offering a simple alternative to template-assisted and liquid-phase hydrothermal methods. Conventional vapor-phase crystal growth often relies on metal substrates to establish locally high pH and ionic gradients.[29,30] In contrast, our method uses only carbonate particles and H_2O_2/H_2O vapor to drive transformation and growth. The resulting structures—spherical aggregates of randomly interwoven γ-MnOOH nanorods—faithfully preserve the morphology of the parent $MnCO_3$ particles, revealing a self-organized pathway to freestanding porous frameworks.

3.2. Self-organized nest-like γ-MnOOH frameworks *via* vapor-assisted conversion

Building on the observation that $MnCO_3$ particles convert into 1D γ-MnOOH aggregates under vapor exposure, we treated $MnCO_3$ powder compacts to realize nest-like porous architectures. The compacts were produced by a hydrothermal hot-pressing strategy that leverages interfacial dissolution–precipitation, thereby avoiding conventional high-temperature sintering and enabling binder-free consolidation with minimal water.[18] Under optimized conditions, the spherical morphology of $MnCO_3$ was preserved during consolidation (Fig. S6).

Upon exposure to H_2O_2/H_2O vapor generated from 5–30% aqueous H_2O_2 at 200 °C for 12 h, $MnCO_3$ pellets underwent phase conversion to γ-MnOOH (Fig. 3A). Single-phase γ-MnOOH was obtained at 5–10% H_2O_2 vapor, whereas higher concentrations promoted further oxidation and dehydration, yielding Mn-oxide by-products (β-MnO_2 and α-Mn_2O_3). Under water vapor, Mn_3O_4 was the dominant product. Surface analysis revealed that water vapor disrupted the spherical $MnCO_3$ morphology, whereas H_2O_2 vapor promoted the anisotropic

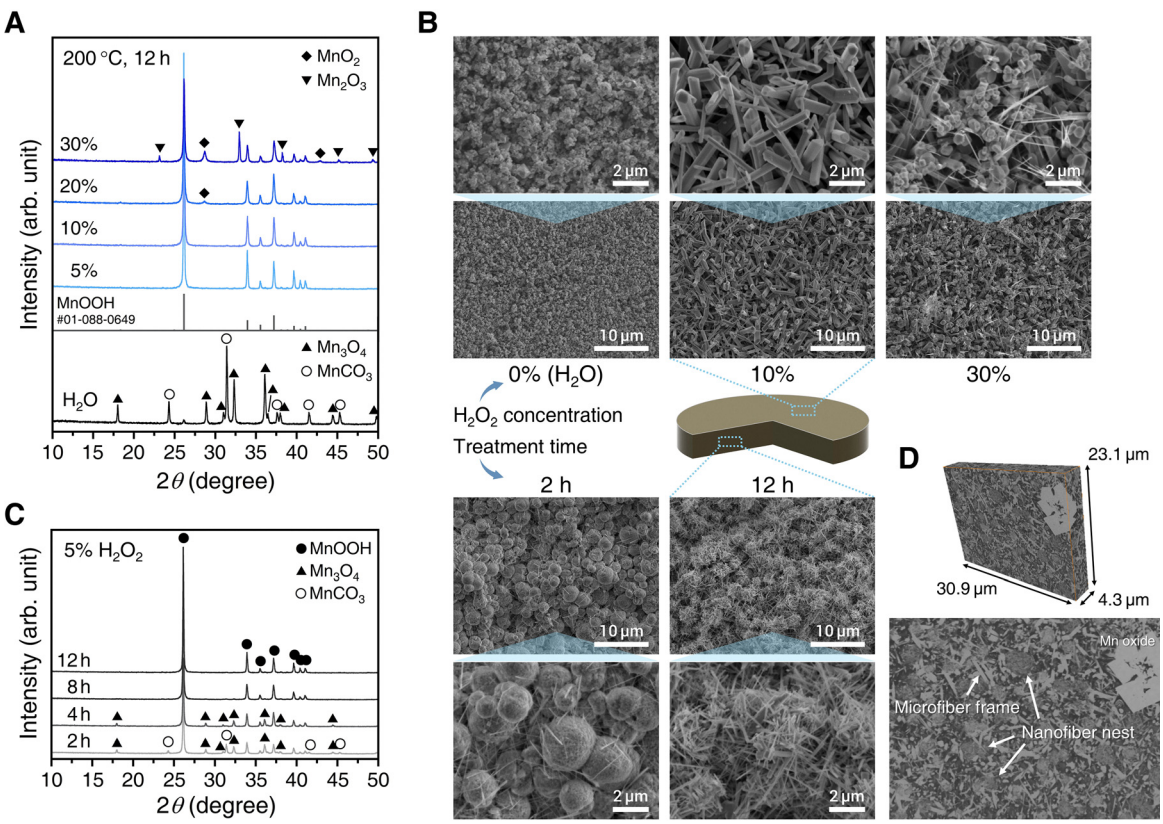

Fig. 3 Nest-like porous γ-MnOOH produced by vapor-assisted conversion: fabrication and characterization. (A) XRD patterns of samples treated with water or 5–30% H_2O_2 vapor. (B) SEM images of $MnCO_3$ powder compacts after vapor treatment: (upper) surface regions after 12 h at varying H_2O_2 concentrations; (lower) interior regions for 2 and 12 h at 5% H_2O_2 vapor. (C) Time-series XRD patterns of samples exposed to 5% H_2O_2 vapor. (D) FIB-SEM 3D reconstruction of the nest-like porous γ-MnOOH architecture obtained after 16 h at 5% H_2O_2.

1D growth of γ-MnOOH (Fig. 3B, upper). The resulting γ-MnOOH microrods (length ≈5 μm) formed interlocked networks with occasional branching. At 30% H_2O_2, angular nanoparticles (350–750 nm) appeared alongside the transition from rod-like γ-MnOOH to nanowire structures. Nanowires were formed *via* tip-directed elongation and, in some cases, by the longitudinal splitting of γ-MnOOH microrods (Fig. S7). Structurally, γ-MnOOH comprises chains of corner-sharing $Mn^{3+}O_6$ octahedra forming proton-containing 1 × 1 rhombohedral tunnels,[31] whereas β-MnO_2 adopts a rutile-type framework of $Mn^{4+}O_6$ octahedra that is structurally related to γ-MnOOH, facilitating preferential formation *via* oxidative decomposition.[32–34] Accordingly, the nanowires derived from γ-MnOOH were identified as β-MnO_2, and the angular nanoparticles were assigned to cubic α-Mn_2O_3.

In contrast to surfaces continuously exposed to H_2O_2 vapor, internal conversion and crystal growth proceeded gradually. Near-surface $MnCO_3$ decomposes rapidly at early stages, yielding γ-MnOOH and transient Mn_3O_4 (Fig. 3C); continuous H_2O_2 supply converts Mn_3O_4 onward to γ-MnOOH.[35] Inside, spherical $MnCO_3$ persisted owing to preferential H_2O_2 consumption at the surface (Fig. 3B, lower). The surface evolved into a rod-like framework that enhanced vapor penetration, while fibrous γ-MnOOH nucleated on the remaining spherical cores. With prolonged exposure, these features transformed into spherical aggregates composed of 1D γ-MnOOH. Notably, the internally formed γ-MnOOH exhibited smaller minor axes than the surface-grown crystals, indicating differences in the growth kinetics arising from gradients in vapor permeability and H_2O_2 concentration. As H_2O_2 is consumed during $MnCO_3$ conversion and γ-MnOOH growth, its concentration decreases in depth. Early stage fibrous γ-MnOOH increases vapor access and promotes the development of microfibers and rod-like γ-MnOOH surrounding spherical nanofiber aggregates. FIB-SEM reveals a seamless internal architecture in which spherical nanofiber aggregates are embedded within a microfiber framework (Fig. 3D and Movie S1), yielding a hierarchical, nest-like porous structure that emerges spontaneously from spatially varying growth rates.

The pore architecture of the nest-like γ-MnOOH was quantified using mercury intrusion porosimetry. The pore size distributions of the samples treated with 5 and 10% H_2O_2 vapor exhibited two key trends (Fig. 4A): (i) the average pore size increased with the H_2O_2 concentration and (ii) the distributions

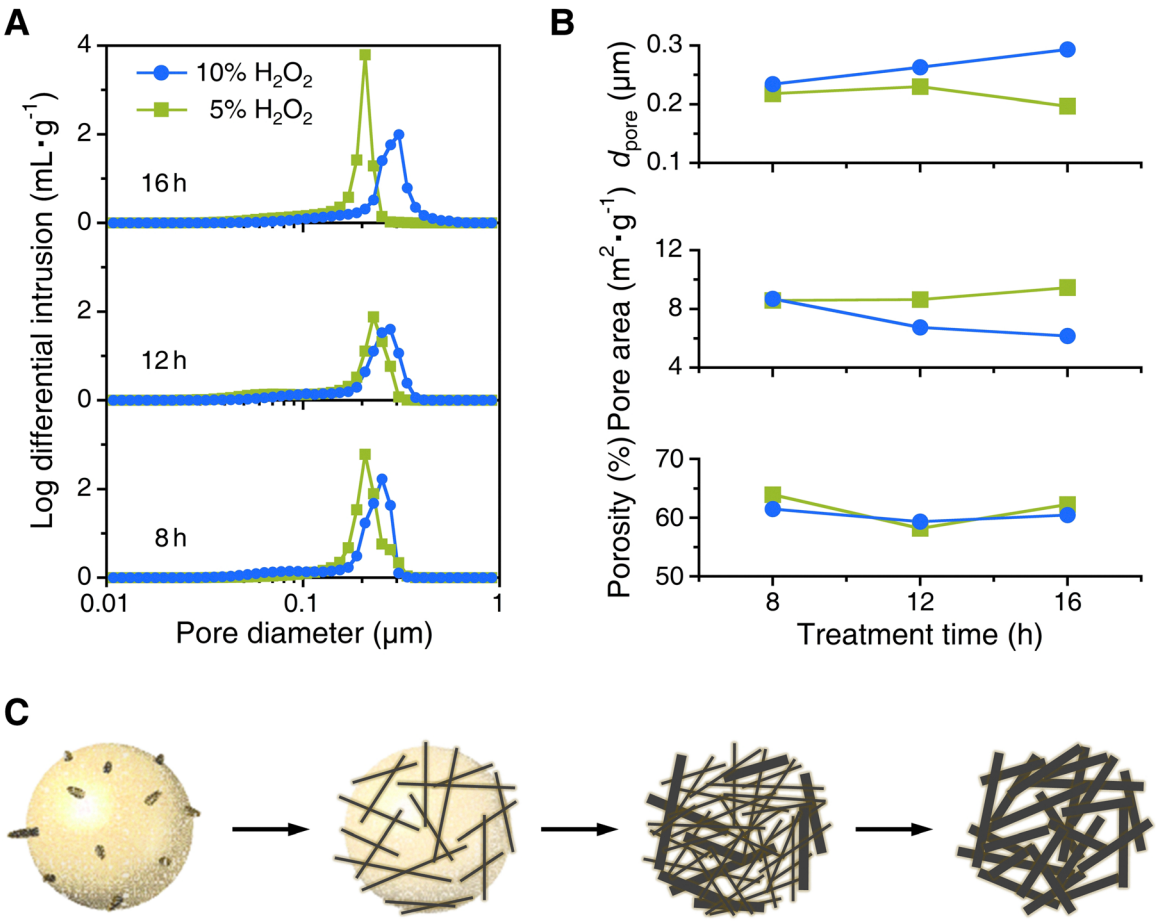

Fig. 4 Pore structure and vapor-phase conversion of nest-like γ-MnOOH. (A) Pore size distributions for samples exposed for 8–16 h to 5 and 10% H_2O_2 vapor. (B) Quantitative analysis of porosity, pore surface area, and mean pore diameter. (C) Schematic of the vapor-phase conversion of spherical $MnCO_3$ to nest-like porous γ-MnOOH *via* solid–gas interfacial reactions.

narrowed with longer exposure. The porosity, pore surface area, and average pore size were further analyzed (Fig. 4B). Assuming a bulk density of ≈ 1.53 g cm^{-3} (geometric determination), the porosity remained broadly constant (58–64%), consistent with the values obtained using the Archimedes method in water (58–65%). In contrast, the pore surface area and pore size were strongly concentration-dependent, with higher H_2O_2 concentrations accelerating the conversion of $MnCO_3$ to γ-MnOOH and promoting more uniform crystal growth, yielding narrower pore distributions and more uniform pores enclosed by interwoven γ-MnOOH nanorods. As growth proceeded, the γ-MnOOH aspect ratios decreased, reducing the pore surface area and increasing the average pore size.

Overall, the nest-like porous architecture forms *via* the vapor-phase conversion of spherical $MnCO_3$ particles, producing aggregates that retained the parent spherical morphology (Fig. 4C). Gradients in the H_2O_2 vapor concentration and exposure time between the surface and interior introduce a temporal offset in growth, resulting in a hierarchical framework composed of a microfiber skeleton interlaced with spherical aggregates of γ-MnOOH nanorods. This outcome is governed by the interplay between vapor transport, reaction kinetics, and morphological evolution. The initial packing density of the $MnCO_3$ compact is also expected to influence this outcome. Higher packing density steepens the H_2O_2 concentration gradient and deepens the structural heterogeneity between the surface and interior, whereas lower packing density permits more uniform vapor penetration. In this study, hydrothermal hot-pressing[18] was employed to achieve reproducible packing with preserved spherical morphology (Fig. S6), ensuring consistent packing density across samples (relative density ≈57%).

3.3. Transport and wetting control in nest-like architectures enabling three-phase separation

The functional advantages of nest-like porous architectures arise from intricately interwoven branches that promote liquid permeability and vapor/gas transport. When the constituent material is intrinsically hydrophobic, water-repellency emerges

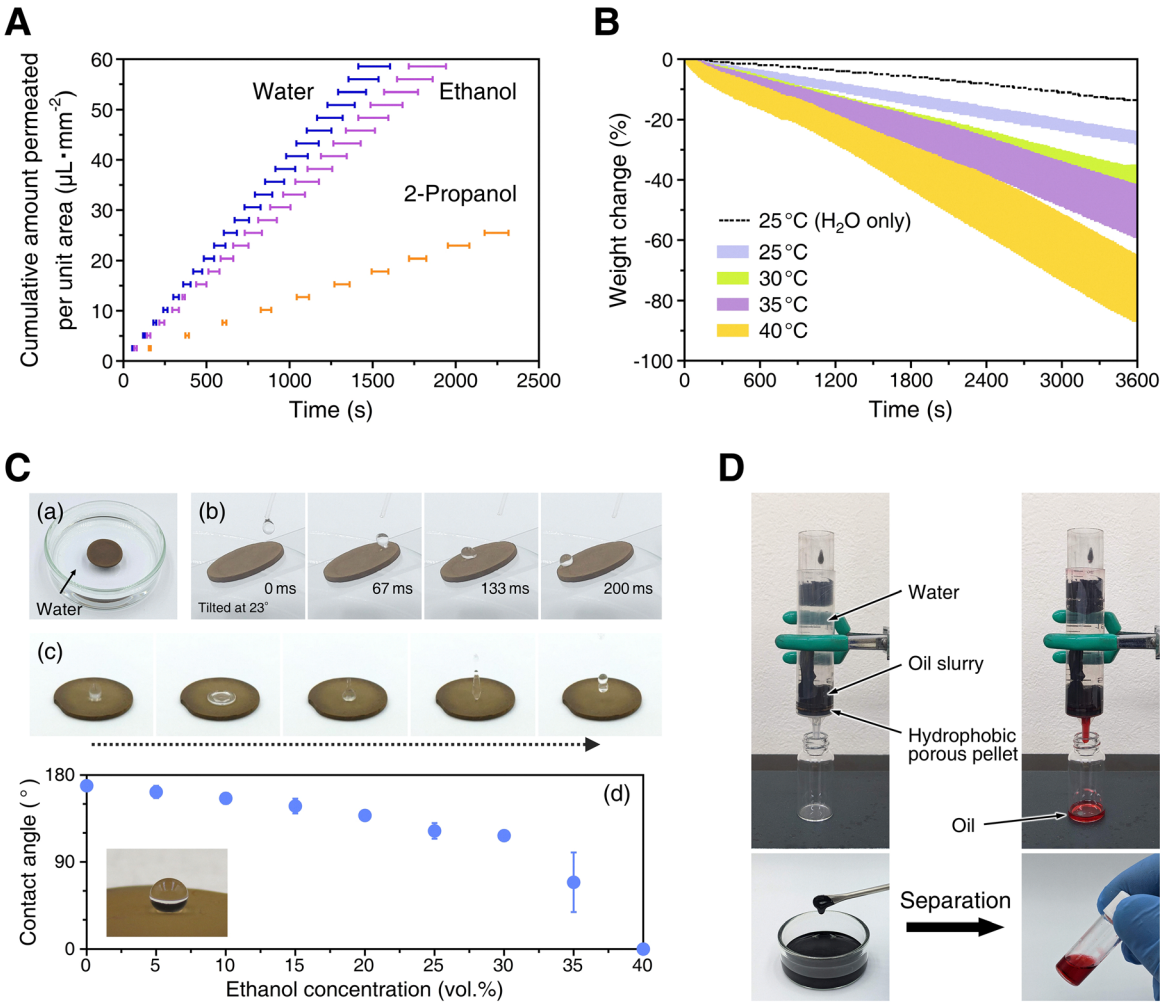

Fig. 5 Transport and wetting control in nest-like γ-MnOOH frameworks. (A) Filtration-based liquid permeability for water, ethanol, and 2-propanol. (B) Water evaporation at a controlled temperature. (C) Hydrophobic modification and wetting response: (a) floating, (b) droplet rolling, (c) vertical drop rebound, and (d) contact angles for water–ethanol mixtures. (D) Three-phase (water/oil/solid) separation of an oil slurry using hydrophobic nest-like γ-MnOOH.

without additional texturing.[36] Motivated by this structure-function interplay, we evaluated the liquid permeation behavior, evaporation performance, wetting control *via* hydrophobic treatment, and application potential of nest-like γ-MnOOH compacts.

We assembled a simple filtration setup using a fabricated nest-like γ-MnOOH compact (ϕ20 × 1.5 mm) as a membrane (Fig. S8) and assessed the liquid permeability under vacuum filtration at a transmembrane pressure of 20 kPa. The flux was measured for water, ethanol, and 2-propanol (Fig. 5A). The average flux values for water and ethanol were approximately 140 and 115 L m^{-2} h^{-1}, respectively, whereas that for 2-propanol was lower at ≈41 L m^{-2} h^{-1}. Notably, the water flux exceeds that of ceramic nanomembranes.[37,38] Given prior reports that surface polarity in pores larger than 100 nm does not significantly influence solvent transport,[39] the dominant factor governing flux is likely the liquid viscosity. Indeed, the viscosities of water, ethanol, and 2-propanol at 25 °C are 0.92, 1.08, and 2.06 mPa s, respectively.[39] The corresponding decrease in flux with increasing viscosity indicates that interactions with the particle surfaces during permeation were negligible.

In addition to enabling rapid water permeation, the porous structure accelerates evaporation. We determined the water content gravimetrically for samples loaded with 200 μL of water in a constant-temperature chamber maintained between 25 and 40 °C (Fig. 5B). For water droplets placed on a Petri dish, only 14% of the water evaporated after 1 h at 25 °C. In contrast, when water was impregnated into the porous architecture, it wetted the surface of γ-MnOOH particles. The enlarged thin-film area, together with capillary self-pumping along the particle arrays, markedly enhanced evaporation.[40] At 40 °C, water evaporation ranged from 70% to 88%, corresponding to an estimated flux of 0.45–0.56 L m^{-2} h^{-1}. The 3D, interconnected pore network should facilitate efficient vapor transport by enhancing diffusion and promoting convective flow.[41] Accordingly, forced convection can further increase the evaporation rate.

Nest-like γ-MnOOH compacts were readily rendered hydrophobic *via* silane coupling by leveraging surface hydroxyl groups. Exposure to trimethoxy(methyl)silane vapor introduced methyl groups onto the particle surfaces. FTIR spectroscopy revealed weak bands attributable to the Si–CH_3 group: a C–H bending mode at 1276 cm^{-1} and a stretching mode at 780 cm^{-1} (Fig. S9). The formation of Si–CH_3 groups weakened hydrogen bonding between surface hydroxyls, shifting the hydrogen-bond bands centered at 2565 cm^{-1} and the combination band with Mn–O at 1940 cm^{-1} to higher wavenumbers.[42] Owing to the resulting hydrophobicity, the porous architecture floated on water (Fig. 5C(a)). When slightly tilted, water droplets rolled off (Fig. 5C(b)), and vertically dropped droplets rebounded without adhesion (Fig. 5C(c) and Movie S2). The hydrophobic nest-like γ-MnOOH architectures exhibited a static water contact angle of 169°, indicative of a superhydrophobic character (Fig. 5C(d)). The 1D-grown γ-MnOOH particles produced a rough surface that supported a Cassie–Baxter-type "lotus effect",[43,44] resulting in an excellent water-repellent surface. Because the contact angle is governed by interfacial energies at the solid–liquid–gas boundaries and depends on the liquid surface tension (σ), we investigated wetting using water–ethanol mixtures. Relative to pure water (σ = 72.8 mN m^{-1} at 20 °C), the surface tension of the mixtures decreases asymptotically with increasing ethanol content (pure ethanol: 22.3 mN m^{-1}).[45] In response, the contact angle decreased approximately linearly up to 30 vol% ethanol, while a hydrophobic state with a contact angle of ≈117° was retained. At ethanol contents exceeding 35 vol%, droplets began to penetrate the substrate; at 40 vol% they fully infiltrated.

Exploiting the differences in surface tension that govern liquid permeability, we further demonstrated the three-phase (water/oil/solid) separation of an oil slurry using a hydrophobically modified, nest-like γ-MnOOH compact (Fig. 5D). We prepared a slurry by mixing hydrophobized spherical Fe_3O_4 particles (≈1 μm in diameter) with red-dyed oil, producing a black slurry. Upon introduction into water, the slurry settled and accumulated on the hydrophobic pellet. The Fe_3O_4 spheres were retained on the pellet surface (Fig. S10), whereas only the oil permeated the porous network and was extracted. This proof-of-concept separation indicates potential utility for collecting or recovering microplastic–oil–dispersant aggregates that form in marine environments.[46–48] By tailoring the surface chemistry of porous architectures and tuning liquid properties (*e.g.*, viscosity and surface tension), diverse applications based on selective permeation, evaporation, and water repellency are enabled. Beyond environmental purification, potential uses include solar-driven seawater desalination[49] and adaptive insulation materials responsive to ambient conditions.[50] The free-standing pellets maintained structural integrity without cracking or disintegration during filtration (20 kPa), evaporation testing, and three-phase separation, demonstrating that the physical entanglement of high-aspect-ratio nanorods provides sufficient cohesion for practical use, although formal mechanical testing remains a subject for future work. No degradation of the porous framework was observed under the mild operating conditions employed here; for more chemically demanding environments, thermal transformation of γ-MnOOH into MnO_2 or Mn_2O_3 offers a route to enhanced chemical stability while retaining the porous architecture.

4. Conclusion

In summary, we established a bio-inspired synthetic strategy to realize freestanding, breathable porous architectures in which structural robustness arises from the extensive entanglement of high-aspect-ratio γ-MnOOH nanorods. Vapor-assisted oxidative conversion drives tip-directed elongation and spontaneous branching, yielding binder-free hierarchical nest-like frameworks directly from $MnCO_3$ precursors. These architectures combine high water permeability (≈140 L m^{-2} h^{-1}), rapid evaporation (0.45–0.56 L m^{-2} h^{-1} at 40 °C under static conditions), and superhydrophobicity (contact angle of 169° after

surface modification), enabling efficient three-phase (water/oil/solid) separation. This scalable platform, rooted in the design logic of nature, offers a versatile route to oxyhydroxide-derived functional materials for applications ranging from thermal management to biocompatible scaffolds.

Author contributions

Takahiro Kozawa: conceptualization, funding acquisition, investigation, methodology, project administration, resources, supervision, validation, visualization, writing – original draft, writing – review & editing. Kayo Fukuyama: investigation. Minoru Osada: writing – review & editing. Hiroya Abe: funding acquisition, methodology, supervision, writing – original draft, writing – review & editing.

Conflicts of interest

The authors declare no conflict of interest.

Data availability

The data supporting the findings of this study are available within this article and its supplementary information (SI). Supplementary information is available: photos, characterization including XRD, crystalline phase ratio, SEM, TEM, and FTIR, filtration device, and movies for FIB-SEM and hydrophobic nature. See DOI: https://doi.org/10.1039/d6ma00109b.

Acknowledgements

This work was funded by the Environmental Research and Technology Development Fund (JPMEERF20211R04), Environmental Restoration and Conservation Agency (ERCA), Grand-in-Aid for Scientific Research KAKENHI (24K21675, 24K01180), Japan Society for the Promotion of Science (JSPS), and the Cooperative Research Project of Design & Engineering by Joint Inverse Innovation for Materials Architecture (DEJI^{2}MA), MEXT. This work was partially conducted through the Joint Usage/Research Program of the Institute of Materials and Systems for Sustainability, Nagoya University.

References

1 Y. Bhosale, N. Weiner, A. Butler, S. H. Kim, M. Gazzola and H. King, Micromechanical origin of plasticity and hysteresis in nestlike packings, *Phys. Rev. Lett.*, 2022, **128**, 198003, DOI: 10.1103/PhysRevLett.128.198003.

2 G. M. Leighton, Evolutionary mechanisms maintaining nest construction in avian clades, *Avian Biol. Res.*, 2016, **9**, 44–51, DOI: 10.3184/175815516X14500793412915.

3 L. Biddle, A. M. Goodman and D. C. Deeming, Construction patterns of birds' nests provide insight into nest-building behaviours, *PeerJ*, 2017, **5**, e3010, DOI: 10.7717/peerj.3010.

4 D. C. Deeming, How does the bird-nest incubation unit work?, *Avian Biol. Res.*, 2016, **9**, 103–113, DOI: 10.3184/175815516X14567543242701.

5 P. Ball, Roles of the nest, *Nat. Mater.*, 2022, **21**, 610, DOI: 10.1038/s41563-022-01280-8.

6 Y. Si, X. Wang, L. Dou, J. Yu and B. Ding, Ultralight and fire-resistant ceramic nanofibrous aerogels with temperature-invariant superelasticity, *Sci. Adv.*, 2018, **4**, eaas8925, DOI: 10.1126/sciadv.aas8925.

7 C. Jia, L. Li, Y. Liu, B. Fang, H. Ding, J. Song, Y. Liu, K. Xiang, S. Lin, Z. Li, W. Si, B. Li, X. Sheng, D. Wang, X. Wei and H. Wu, Highly compressible and anisotropic lamellar ceramic sponges with superior thermal insulation and acoustic absorption performances, *Nat. Commun.*, 2020, **11**, 3732, DOI: 10.1038/s41467-020-17533-6.

8 H. J. Kwon, D. S. Yang, M. S. Koo, S. M. Ji, J. Jeong, S. Oh, S. K. Kuk, H. Heo, D. J. Ham, M. Kim, H. Choi, J.-M. Lee, J.-W. Shur, W.-J. Lee, C.-O. Bin, N. Timofeev, H. Wu, L. Wang, T. Lee, D. J. Jacob and H. C. Lee, Long-lifetime water-washable ceramic catalyst filter for air purification, *Nat. Commun.*, 2023, **14**, 520, DOI: 10.1038/s41467-023-36050-w.

9 X. Zhou, R. Shevate, D. Huang, T. Cao, X. Shen, S. Hu, A. U. Mane, J. W. Elam, J.-H. Kim and M. Elimelech, Ceramic thin-film composite membranes with tunable sub-nanometer pores for molecular sieving, *Nat. Commun.*, 2023, **14**, 7255, DOI: 10.1038/s41467-023-42495-w.

10 H. Wang, J. Tian, Y. Jiang, S. Liu, J. Zheng, N. Li, G. Wang, F. Dong, J. Chen, Y. Xie, Y. Huang, X. Cai, X. Wang, W. Xiong, H. Qi, L. Yin, Y. Wang and X. Sheng, A 3D biomimetic optoelectronic scaffold repairs cranial defects, *Sci. Adv.*, 2023, **9**, eabq7750, DOI: 10.1126/sciadv.abq7750.

11 H. Wang, X. Zhang, N. Wang, Y. Li, X. Feng, Y. Huang, C. Zhao, Z. Liu, M. Fang, G. Ou, H. Gao, X. Li and H. Wu, Ultralight, scalable, and high-temperature–resilient ceramic nanofiber sponges, *Sci. Adv.*, 2017, **3**, e1603170, DOI: 10.1126/sciadv.1603170.

12 Y. Zhang, S. Liu, J. Yan, X. Zhang, S. Xia, Y. Zhao, J. Yu and B. Ding, Superior flexibility in oxide ceramic crystal nanofibers, *Adv. Mater.*, 2021, **33**, 2105011, DOI: 10.1002/adma.202105011.

13 C. Hu, S. Jahan, B. Yuan and R. Panat, 3D-AJP: Fabrication of advanced microarchitected multimaterial ceramic structures via binder-free and auxiliary-free aerosol jet 3D nanoprinting, *Adv. Sci.*, 2025, **12**, 2405334, DOI: 10.1002/advs.202405334.

14 C. Ferraro, E. Garcia-Tuñon, V. G. Rocha, S. Barg, M. D. Fariñas, T. E. G. Alvarez-Arenas, G. Sernicola, F. Giuliani and E. Saiz, Light and strong SiC networks, *Adv. Funct. Mater.*, 2016, **26**, 1489, DOI: 10.1002/adfm.201504051.

15 J. V. John, A. McCarthy, H. Wang, Z. Luo, H. Li, Z. Wang, F. Cheng, Y. S. Zhang and J. Xie, Freeze-casting with 3D-printed templates creates anisotropic microchannels and patterned macrochannels within biomimetic nanofiber aerogels for rapid cellular infiltration, *Adv. Healthcare Mater.*, 2021, **10**, 2100238, DOI: 10.1002/adhm.202100238.

16 H. Bai, Y. Chen, B. Delattre, A. P. Tomsia and R. O. Ritchie, Bioinspired large-scale aligned porous materials assembled with dual temperature gradients, *Sci. Adv.*, 2015, **1**, e1500849, DOI: 10.1126/sciadv.1500849.

17 T. Kozawa, K. Yanagisawa, T. Murakami and M. Naito, Growth behavior of $LiMn_2O_4$ particles formed by solid-state reactions in air and water vapor, *J. Solid State Chem.*, 2016, **243**, 241–246, DOI: 10.1016/j.jssc.2016.08.033.

18 T. Kozawa, Microstructural development of $MnCO_3$ microsphere compacts through hydrothermal hot-pressing, *J. Eur. Ceram. Soc.*, 2022, **42**, 1530, DOI: 10.1016/j.jeurceramsoc.2021.12.022.

19 M. Y. Alkawareek, B. M. Akkelah, S. M. Mansour, H. M. Amro, S. R. Abulateefeh and A. M. Alkilany, Simple experiment to determine surfactant critical micelle concentrations using contact-angle measurements, *J. Chem. Educ.*, 2018, **95**, 2227, DOI: 10.1021/acs.jchemed.8b00276.

20 S.-H. Do, B. Batchelor, H.-K. Lee and S.-H. Kong, Hydrogen peroxide decomposition on manganese oxide (pyrolusite): Kinetics, intermediates, and mechanism, *Chemosphere*, 2009, **75**, 8, DOI: 10.1016/j.chemosphere.2008.11.075.

21 C. M. Lousada, A. J. Johansson, T. Brinck and M. Jonsson, Mechanism of H_2O_2 decomposition on transition metal oxide surfaces, *J. Phys. Chem. C*, 2012, **116**, 9533, DOI: 10.1021/jp300255h.

22 T. Gao, F. Krumeich, R. Nesper, H. Fjellvåg and P. Norby, Microstructures, surface properties, and topotactic transitions of manganite nanorods, *Inorg. Chem.*, 2009, **48**, 6242, DOI: 10.1021/ic900565m.

23 H. Zhang, C. Liang, Z. Tian, G. Wang and W. Cai, Organization of Mn_3O_4 nanoparticles into γ-MnOOH nanowires *via* hydrothermal treatment of the colloids induced by laser ablation in water, *CrystEngComm*, 2011, **13**, 1063, DOI: 10.1039/c004482b.

24 S. Sarkar, S. Sarkar and A. K. Patra, Single crystalline manganite (γ-MnOOH) rods enclosed with high index facets and its excellent catalytic conversion of lignin-derived feedstock, *J. Solid State Chem.*, 2022, **315**, 123444, DOI: 10.1016/j.jssc.2022.123444.

25 D. Zheng, Z. Yin, W. Zhang, X. Tan and S. Sun, Novel branched γ-MnOOH and β-MnO_2 multipod nanostructures, *Cryst. Growth Des.*, 2006, **6**, 1733, DOI: 10.1021/cg060223m.

26 Y. Mi, X. Zhang, Z. Yang, Y. Li, S. Zhou, H. Zhang, W. Zhu, D. He, J. Wang and G. Van Tendeloo, Shape selective growth of single crystalline MnOOH multipods and 1D nanowires by a reductive hydrothermal method, *Mater. Lett.*, 2007, **61**, 1781, DOI: 10.1016/j.matlet.2006.07.130.

27 Y. Li, H. Tan, O. Lebedev, J. Verbeeck, E. Biermans, G. Van Tendeloo and B.-L. Su, Insight into the growth of multiple branched MnOOH nanorods, *Cryst. Growth Des.*, 2010, **10**, 2969, DOI: 10.1021/cg100009k.

28 C.-C. Hu, Y.-T. Wu and K.-H. Chang, Low-temperature hydrothermal synthesis of Mn_3O_4 and MnOOH single crystals: Determinant influence of oxidants, *Chem. Mater.*, 2008, **20**, 2890, DOI: 10.1021/cm703245k.

29 P. Liu, H. Zhang, H. Liu, Y. Wang, X. Yao, G. Zhu, S. Zhang and H. Zhao, A facile vapor-phase hydrothermal method for direct growth of titanate nanotubes on a titanium substrate via a distinctive nanosheet roll-up mechanism, *J. Am. Chem. Soc.*, 2011, **133**, 19032, DOI: 10.1021/ja207530e.

30 H. Zhang, Y. Li, P. Liu, Y. Li, D. Yang, H. Yang and H. Zhao, A new vapor-phase hydrothermal method to concurrently grow ZnO nanotube and nanorod array films on different sides of a zinc foil substrate, *Chem. – Eur. J.*, 2012, **18**, 5165, DOI: 10.1002/chem.201200036.

31 P. F. Smith, B. J. Deibert, S. Kaushik, G. Gardner, S. Hwang, H. Wang, J. F. Al-Sharab, E. Garfunkel, L. Fabris, J. Li and G. C. Dismukes, Coordination geometry and oxidation state requirements of corner-sharing MnO_6 octahedra for water oxidation catalysis: An investigation of manganite (γ-MnOOH), *ACS Catal.*, 2016, **6**, 2089, DOI: 10.1021/acscatal.6b00099.

32 G. Xi, Y. Peng, Y. Zhu, L. Xu, W. Zhang, W. Yu and Y. Qian, Preparation of β-MnO_2 nanorods through a γ-MnOOH precursor route, *Mater. Res. Bull.*, 2004, **39**, 1641, DOI: 10.1016/j.materresbull.2004.05.014.

33 Z. Yang, Y. Zhang, W. Zhang, X. Wang, Y. Qian, X. Wen and S. Yang, Nanorods of manganese oxides: Synthesis, characterization and catalytic application, *J. Solid State Chem.*, 2006, **179**, 679, DOI: 10.1016/j.jssc.2005.11.028.

34 F. Li, J. Wu, Q. Qin, Z. Li and X. Huang, Facile synthesis of γ-MnOOH micro/nanorods and their conversion to β-MnO_2, Mn_3O_4, *J. Alloys Compd.*, 2010, **492**, 339, DOI: 10.1016/j.jallcom.2009.11.089.

35 C. J. Lind, Hausmannite (Mn_3O_4) conversion to manganite (γ-MnOOH) in dilute oxalate solution, *Environ. Sci. Technol.*, 1988, **22**, 62, DOI: 10.1021/es00166a006.

36 L. E. Biddle, A. M. Dickinson, R. E. Broughton, L. A. Gray, S. L. Bennett, A. M. Goodman and D. C. Deeming, Construction materials affect the hydrological properties of bird nests, *J. Zool.*, 2019, **309**, 161–171, DOI: 10.1111/jzo.12713.

37 S. Benfer, P. Árki and G. Tomandl, Ceramic membranes for filtration applications—Preparation and characterization, *Adv. Eng. Mater.*, 2004, **6**, 495–500, DOI: 10.1002/adem.200400577.

38 S. Y. Yang, I. Ryu, H. Y. Kim, J. K. Kim, S. K. Jang and T. P. Russell, Nanoporous membranes with ultrahigh selectivity and flux for the filtration of viruses, *Adv. Mater.*, 2006, **18**, 709–712, DOI: 10.1002/adma.200501500.

39 A. Buekenhoudt, F. Bisignano, G. De Luca, P. Vandezande, M. Wouters and K. Verhulst, Unravelling the solvent flux behaviour of ceramic nanofiltration and ultrafiltration membranes, *J. Membr. Sci.*, 2013, **439**, 36–47, DOI: 10.1016/j.memsci.2013.03.032.

40 G. Jiang, L. Wang, Z. Tian, C. Chen, X. Hu, R. Peng, D. Li, H. Zhang, P. Fan and M. Zhong, Boosting water evaporation *via* continuous formation of a 3D thin film through triple-level super-wicking routes, *Mater. Horiz.*, 2023, **10**, 3523–3535, DOI: 10.1039/D3MH00548H.

41 J. Li, Z. Wang, Z. Lin, N. Xu, X. Li, J. Liang, W. Zhao, R. Lin, B. Zhu, G. Liu, L. Zhou, S. Zhu and J. Zhu, Over 10 kg m^{-2} h^{-1} evaporation rate enabled by a 3D interconnected porous carbon foam, *Joule*, 2020, **4**, 928–937, DOI: 10.1016/j.joule.2020.02.014.

42 E. Libowitzky, Correlation of O-H stretching frequencies and O-H. . .O hydrogen bond lengths in minerals, *Monatsh. Chem.*, 1999, **130**, 1047–1059, DOI: 10.1007/BF03354882.
43 T. Onda, S. Shibuichi, N. Satoh and K. Tsujii, Super-water-repellent fractal surfaces, *Langmuir*, 1996, **12**, 2125–2127, DOI: 10.1021/la950418o.
44 N. A. Patankar, Mimicking the lotus effect: Influence of double roughness structures and slender pillars, *Langmuir*, 2004, **20**, 8209–8213, DOI: 10.1021/la048629t.
45 G. Vazquez, E. Alvarez and J. M. Navaza, Surface tension of alcohol water + water from 20 to 50 °C, *J. Chem. Eng. Data*, 1995, **40**, 611–614, DOI: 10.1021/je00019a016.
46 M. Yang, B. Zhang, X. Xin, B. Liu, Z. Zhu, G. Dong, Y. Zhao, K. Lee and B. Chen, Microplastic-oil-dispersant agglomerates in the marine environment: Formation mechanism and impact on oil dispersion, *J. Hazard. Mater.*, 2022, **426**, 127825, DOI: 10.1016/j.jhazmat.2021.127825.
47 M. Yang, B. Zhang, X. Chen, Q. Kang, B. Gao, K. Lee and B. Chen, Transport of microplastic and dispersed oil co-contaminants in the marine environment, *Environ. Sci. Technol.*, 2023, **57**, 5633–5645, DOI: 10.1021/acs.est.2c08716.
48 H. Hong, R. S. Bang, L. Verster and O. D. Velev, Designing of self-dispersing soft dendritic microcleaners for microplastics capture and recovery, *Adv. Funct. Mater.*, 2025, **35**, 2423494, DOI: 10.1002/adfm.202423494.
49 X. Song, L. Jia, Z. Wei, T. Xiang and S. Zhou, Nature-inspired sustainable solar evaporators for seawater desalination, *J. Mater. Chem. A*, 2024, **12**, 613–633, DOI: 10.1039/d3ta05941c.
50 L. Zheng, Y. Zuo, X. Li and Y. Wu, Biomimetic swallow nest structure: A lightweight and high-strength thermal insulation material, *ACS Nano*, 2022, **16**, 8116–8127, DOI: 10.1021/acsnano.2c01451.